RAPID COMMUNICATIONS

PHYSICAL REVIEW A VOLUME 35, NUMBER 7 APRIL 1, 1987

Density matrix for the H($n=3$) atoms formed in electron-capture process of H^+-helium collisions at 25–100 keV

Ashok Jain and C. D. Lin
Physics Department, Cardwell Hall, Kansas State University, Manhattan, Kansas 66506

W. Fritsch
Bereich Kern- und Strahlenphysik, Hahn-Meitner-Institut Berlin GmbH, D-1000 Berlin 39, West Germany
(Received 3 November 1986)

The full $n=3$ density matrices of hydrogen atoms formed after electron capture in H^+-He collisions at 25–100 keV are calculated in a modified two-center atomic-orbital close-coupling expansion method. The integrated (over impact parameters) density matrix and its first-order moments are compared with recent experimental results. A charge-density plot is used to illustrate that the electron is lagging behind the projectile after the capture in the energy range considered. From the differential density matrix analysis, a "classical" orbital picture of the captured electron is proposed.

The density-matrix formalism provides a complete characterization of collisionally produced excited atoms. For hydrogenic excited final states, the full density matrix within a given n manifold can be determined experimentally by measuring the four Stoke's parameters of the emitted radiation as a function of applied external electric field. Recently, there has been a considerable experimental effort to determine the full $n=3$ density matrix for the H atoms produced by electron capture in $H^+ + He$ collisions at 40–80 keV.[1–4] Stoke's parameters for the Balmer-α transitions are determined in an axial and in a transverse electric field from which the full density matrix for the $n=3$ manifold has been deduced.[1–4] In a different experiment, the diagonal elements of the H($n=3$) density matrix have also been measured[5] by observing the Balmer-α emitted light from the final atoms which pass through a radio-frequency field after the collision process.

The above experiments have certain practical difficulties in deducing the final density-matrix elements. In the experiment of Brower and Pipkin[5] the major source of error for partial *nlm* cross sections is derived from cascading effects, while in the work of Havener and co-workers[1–3] and Stone[4] the difficulty is in the numerical fitting procedure for obtaining accurately the 14 unknown density-matrix parameters. Theoretically, the complete density matrix for the $n=3$ level of H atoms has been calculated in higher-Born and in the continuum distorted-wave (CDW) approximations.[6] There have been questions concerning whether these high-energy methods can be applied to deduce charge-transfer parameters at the intermediate energies carried out in these experiments.

In this Rapid Communication we report the results of a close-coupling calculation of the full n-manifold density matrix for the excited H atoms formed in the $H^+ + He$ charge-transfer process, using a modified two-center atomic-orbital expansion (AO+) model.[7] In this type of close-coupling AO+ calculation, one faces several difficulties. First, the cross sections for the present $n=3$ manifold are quite small compared to the dominant 1s channel. These small channels are greatly affected by target excitation and ionization processes. Second, the final-state mixing of the degenerate hydrogenic levels due to the Stark field of the residual target ion has to be included. Third, we found that a major contribution to electron capture occurs at small impact parameters. This is understood from the "molecular orbital" viewpoint that the dominant mechanism for electron capture is a promotion via low-lying molecular orbitals near the united-atom (UA) limit.[8] In the AO+-type expansion, the Stark mixing of the final states is automatically included in the solution of the close-coupling equations, while the mechanism of promotion via molecular orbitals and the effects of ionization and excitation channels are included by a judicious choice of pseudostates.[7,8]

In this work, each electron in He is treated independently in a model potential.[9] A total of 19 states were used in the AO+ expansion. On the projectile center, there are ten ($n=1$, 2, and 3) hydrogenic states and two 1s pseudostates with exponents 1.5 and 0.5. On the target center, two 1s orbitals with exponents 1.453 and 2.78 represent the He ground state; three 2s, $2p_0$, and $2p_1$, states with exponents 0.25, 1.194, and 1.194, respectively, and two 1s orbitals with exponents 1.5 and 0.5 are also included to represent approximately the target excitation and ionization channels. The precise nature of these pseudostates is not crucial. (We will address this question further in a later publication.) We noted that the capture cross sections to $n=1$, 2, and 3 manifolds and excitation and ionization cross sections obtained from the present basis set are in good agreement with experiments in the 25–100-keV region.[10] In this Rapid Communication we are concerned only with the capture to the $n=3$ manifold.

Although the experimental studies have been performed in the 40–80-keV region, the recent improved data are available only for 60-keV energy.[11,12] We first compare our integrated $n=3$ density matrix at 60 keV with the recent data of Westerveld[11] and Brower[12] groups (only diagonal elements from the later group) in Table I. It is clear from this table that there is good agreement in the whole density matrix except for small channels. From the off-

TABLE I. Integrated density matrix (normalized to the $3s$ cross section) for the $n=3$ manifold of H atoms formed in $H^+ + He$ collisions at 60 keV.

Element	Present	Expt. (Ref. 11)	Expt. (Ref. 12)
s_0	1.0	1.0	1.0
s_0p_0	$0.27-i0.134$	$0.30-i0.05$	. . .
s_0d_0	$0.11+i0.02$	$0.09-i0.05$	. . .
p_0	0.232	0.22	0.16
p_1	0.012	+0.014	0.06
p_0d_0	$0.062+i0.056$	$0.039+i0.016$	. . .
p_1d_1	$0.004+i0.004$	$0.00+i0.002$	. . .
d_0	0.03	0.03	0.011
d_1	0.0024	$-0.005\hat{5}$	0.018
d_2	0.00014	0.009	−0.001
$\langle D_z\rangle$	3.62	4.08	. . .
$\langle \mathbf{L}\times\mathbf{A}\rangle_{z,s}$	0.1176	0.06	. . .

diagonal elements, we also calculated the averaged values of the z component of the dipole moment $\langle D_z\rangle$ and the velocity vector $\langle \mathbf{L}\times\mathbf{A}\rangle_{z,s}$, where $\mathbf{L}$ is the angular momentum and $\mathbf{A}$ is the Runge-Lenz vector. (For the definition of these parameters, see Ref. 13. Note that both these parameters have been normalized by the trace of the density matrix for the $n=3$ manifold and that z is the quantization axis parallel to the beam direction.) The vector $\mathbf{A}$ (which is proportional to the dipole moment) points from the projectile center to the perihelion of the electronic orbit, while the vector $\mathbf{L}\times\mathbf{A}$ is in the direction of the electronic orbital velocity (see Fig. 3). As shown in Table I, our values are in good agreement with the experimental data. In passing, we mention that the dipole moment calculated using the CDW theory is a factor of 2 smaller.

To examine the energy dependence, we show in Fig. 1 the calculated $\langle D_z\rangle$ and $\langle \mathbf{L}\times\mathbf{A}\rangle_{z,s}$ parameters at 25–100 keV. In this figure, the earlier experimental results[3] for both parameters are shown along with the new value[11] for $\langle D_z\rangle$ at 60 keV. Our calculated values indicate that $\langle \mathbf{L}\times\mathbf{A}\rangle_{z,s}$ changes sign around 90 keV. For comparison, the CDW results[6] for $\langle D_z\rangle$ are shown in dashed lines. The dipole moment for $n=3$ shown in Fig. 1 is positive throughout, which means that the electron cloud lags behind the projectile in the energy range considered. At high velocities, the dipole moment drops rapidly, reflecting that capture to $3p$ and $3d$ states becomes relatively smaller compared with $3s$ channel at these energies. For lower velocities, it acquires a maximum value of 5.4 a.u. at 35 keV (the maximum allowed is 7.35 a.u.).

The density matrix contains all the information extractable from scattering experiments. The two first-order moments discussed above are just the two convenient parameters which offer some simple physical interpretations. To illustrate the electron cloud distribution of the $n=3$ manifold after the collision, we show in the same Fig. 1 density plots at 35- and 60-keV energies. One can see clearly that the electron cloud indeed lags behind the projectile. In fact, the front-behind asymmetry is quite striking. The asymmetry decreases rapidly as the collision velocity increases in agreement with the $\langle D_z\rangle$ curve A (Fig. 1).

To understand the results of Fig. 1 it is necessary to examine the impact-parameter (b) dependence of the above quantities. We display in Fig. 2 the "decomposition" of the dipole moment and the $(\mathbf{L}\times\mathbf{A})_{z,s}$ at 60 keV at each impact parameter. In this case, we can also show the $D_x(b)$. Notice that all quantities in Fig. 2 are not normalized. We note that the $D_z(b)$ is positive at all impact pa-

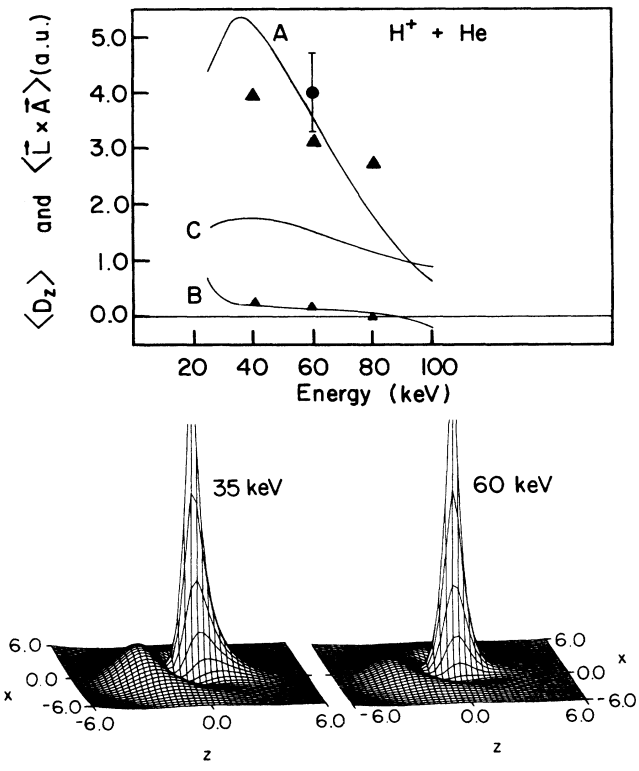

FIG. 1. $\langle D_z\rangle$ (curve A) and $\langle \mathbf{L}\times\mathbf{A}\rangle_{z,s}$ (curve B) at 25–100 keV for the charge transfer $H^+ + He \rightarrow H(n=3) + He^+$ process. The CDW Born calculations (Ref. 6) are shown by curve C. Experimental data: ▲, Ref. 3. ●, Ref. 11. The three-dimensional plots are for the charge density of the captured electron around the projectile in the xz plane at 35- and 60-keV impact energies.

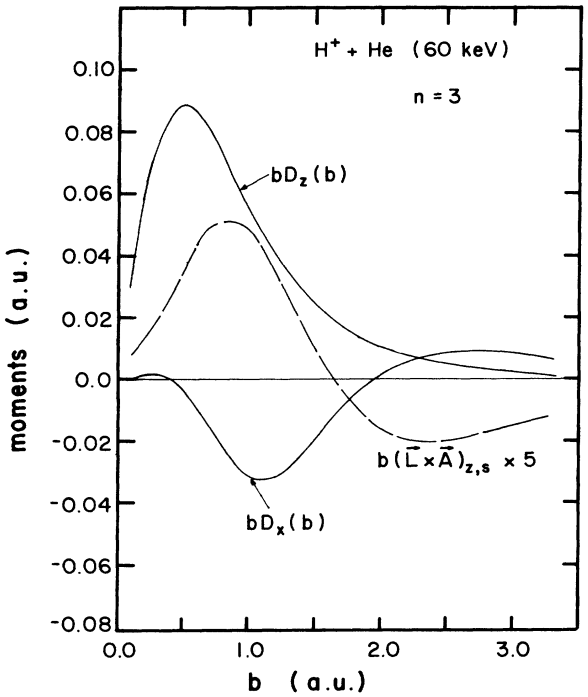

FIG. 2. Calculated b-dependent dipole (D_x and D_z) and $(\mathbf{L}\times\mathbf{A})_{z,s}$ parameters at 60 keV.

rameters, indicating that the center of the electron cloud always lags behind the projectile at all impact parameters. For $D_x(b)$, we note that there is a sign change. At large b, $D_x(b)$ is positive while it is negative for small b. The quantity $(\mathbf{L}\times\mathbf{A})_{z,s}(b)$ is positive for small b and negative for large b; this changeover of sign in its b dependence, in fact, illustrates that the charge cloud and current distributions at the end of the collision are quite different for large- and small-b regions.

In Fig. 3, we sketch a classical analog of the behavior of the quantities $D_x(b)$, $D_z(b)$, and $(\mathbf{L}\times\mathbf{A})_{z,s}(b)$ for small and large b as shown in Fig. 2. Classically, the electron is described by a Kepler orbit. The Kepler orbits of the captured electron, consistent with the calculated D_x, D_z, and $(\mathbf{L}\times\mathbf{A})_{z,s}$, are shown in Fig. 3(a) for small b and in Fig. 3(b) for large-b values. Notice that the speed of the electron is slowest at the aphelion and fastest at the perihelion and that the $(\mathbf{L}\times\mathbf{A})_{z,s}$ is in the direction of the orbital ve-

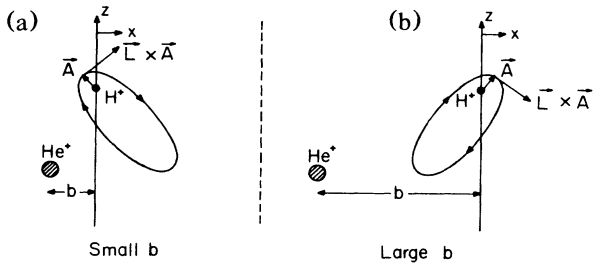

FIG. 3. A "classical" orbital picture of the electron after the capture in the small- and large-b regions.

locity at the perihelion. In Fig. 3(a), the orbit is oriented such that it gives a positive D_z and a negative D_x and the arrows indicating the orbiting direction of the electron are consistent with a positive $(\mathbf{L}\times\mathbf{A})_{z,s}$. In contrast, the orbit and the sense of rotation in Fig. 3(b) correspond to a positive D_z, a positive D_x, and a negative $(\mathbf{L}\times\mathbf{A})_{z,s}$. The above "classical" Kepler orbits are consistent with a simple intuitive picture of electron capture. At large impact parameters, due to short interaction time, we can expect that the electron is pulled towards the projectile throughout the collision time; thus the electron lags behind the projectile nucleus and lies between the two heavy particles. On the other hand, for collisions at small-b values, the electron has to swing back toward the projectile as it overshoots to the right during the early stage of the collision.

In summary, we have shown that the two-center AO+ model allows us to extract detailed information about electron capture to excited states in H^++He collisions at intermediate energies. The calculated integrated density matrix for the $H(n=3)$ manifold at 60 keV is in good agreement with the measured results. By analyzing the differential density matrix in terms of the dipole moments and the velocity vector $(\mathbf{L}\times\mathbf{A})_{z,s}$, we have been able to provide a simple "classical" orbital picture of the average electron density and current distributions after electron capture.

We thank J. Risley, W. Westerveld, C. C. Havener, and M. Brower for useful discussions and for sending us their data prior to publication. This work was supported in part by the U.S. Department of Energy, Office of Energy Research, Division of Chemical Sciences.

[1]C. C. Havener, W. B. Westerveld, J. S. Risley, N. H. Tolk, and J. C. Tully, Phys. Rev. Lett. **48**, 926 (1982).
[2]C. C. Havener, N. Rouze, W. B. Westerveld, and J. S. Risley, Phys. Rev. Lett. **53**, 1049 (1984).
[3]C. C. Havener, N. Rouze, W. B. Westerveld, and J. Risley, Phys. Rev. A **33**, 276 (1986).
[4]C. D. Stone, Master's thesis, North Carolina State University, 1986 (unpublished).
[5]M. C. Brower and F. M. Pipkin, Bull. Am. Phys. Soc. **31**, 994 (1986).
[6]J. Burgdorfer and L. J. Dube, Phys. Rev. Lett. **52**, 2225 (1984).
[7]W. Fritsch and C. D. Lin, Phys. Rev. A **27**, 3361 (1983), and references therein.
[8]M. Kimura and C. D. Lin, Phys. Rev. A **34**, 176 (1986).
[9]L. Opradolce, P. Valiron, and R. McCarrol, J. Phys. B **16**, 2017 (1983).
[10]J. L. Edwards and E. W. Thomas, Phys. Rev. A **2**, 2346 (1976); J. Lenormand, J. Phys. (Paris) **37**, 699 (1976); R. Hippler, W. Harbich, M. Faust, H. O. Lutz, and L. J. Dube, J. Phys. B **19**, 1507 (1986).
[11]W. B. Westerveld (private communication).
[12]M. C. Brower (private communication).
[13]J. Burgdorfer, Z. Phys. A **309**, 285 (1983).